PAPER

Check for updates

Rational design of lanthanide-based metal–organic frameworks for CO$_2$ capture using computational modeling†

Zeynep Pinar Haslak,‡ Hasan Can Gulbalkan [ID] ‡ and Seda Keskin [ID] *

Metal organic frameworks (MOFs) have emerged as promising materials in the context of CO$_2$ capture and separation. Thanks to their tunable nature, various functionalities can be introduced to improve their separation performances. Lanthanide MOFs (Ln-MOFs) with high coordination numbers offer a promising space for the design of new high-performing and stable adsorbents for gas adsorption and separation. In this study, we combined molecular simulations with quantum mechanical (QM) calculations for designing new hypothetical materials offering superior CO$_2$/N$_2$ separation performances. An Ln-MOF having high CO$_2$/N$_2$ selectivity and working capacity was originally selected and its linkers were exchanged with five different types of linkers and its metal atom was exchanged with 12 different Ln^{3+} metals to generate 77 different types of hypothetic Ln-MOFs. Following the initial geometry optimizations at the molecular mechanics (MM) level, these structures were studied for CO$_2$/N$_2$ separation by performing grand canonical Monte Carlo (GCMC) simulations. Five MOFs were found to outperform the original Ln-MOF structure and they were optimized at the QM level to obtain geometries with minimized total energy, which finally led to two hypothetic Ln-MOFs offering superior CO$_2$/N$_2$ separation performance. The computational work that we described in this study will be useful for the rational design of new Ln-based MOFs with improved CO$_2$ separation properties.

1. Introduction

Despite the massive investments and incitements in research to achieve efficient CO$_2$ capture and to reduce greenhouse gas emissions, global CO$_2$ emissions continue to rise.[1] Currently, absorption/scrubbing, adsorption, cryogenic distillation, and membrane-based separation are the leading technologies for CO$_2$/N$_2$ separation. The most widely used technology in the industry for CO$_2$ separation is amine-based scrubbing, despite its several drawbacks, such as the large energy penalty and high solvent volatility.[2–4] Adsorption-based CO$_2$ separation with porous materials has emerged as an alternative since it is reversible and requires less energy than scrubbing.[3]

Metal organic frameworks (MOFs), materials in which inorganic nodes are connected through organic linkers to create highly porous structures, have been considered as a versatile platform for gas adsorption, separation, catalysis, and sensing.[5,6] The greatest advantage of MOFs over conventional porous

materials is that by varying the combination of inorganic nodes and organic linkers, a wide range of MOFs with various pore shapes/sizes and chemical functions can be synthesized. MOFs having desirable functionalities can be generated by modulating the choice of the parent MOF, also known as the genotype MOF, through introducing functional groups to the linker scaffolds,[7–10] linker exchange,[11–13] or metal exchange.[14–16] However, it is not always guaranteed that the designed MOF will be stable after synthesis, its porosity will be permanent, or it will perform better than the parent MOF. Due to the large number of linkers and metal atoms that can be used to design a MOF, synthesis, and performance evaluation of thousands of structures through purely experimental methods is not efficient. Computational methods offer great advantages for the design of new MOFs with high CO$_2$ selectivities at an affordable cost.

Computational studies focusing on HKUST-1,[17] IRMOFs,[18] and ZnO-MOFs[19] reported the significance of metal-exchange in achieving increased CO$_2$ adsorption capacity. The impact of ligand functionalization in MOFs was also computationally evaluated for MOF-74, MIL-53, UiO-66, UiO-67,[20] and multivariate MOFs,[21] and results showed that ligand functionalization can improve the CO$_2$ affinity of the MOFs. On the other hand, linker exchange and its impact on the gas affinity of

Department of Chemical and Biological Engineering, Koc University, Rumelifeneri Yolu, Sariyer, 34450 Istanbul, Turkey. E-mail: skeskin@ku.edu.tr;
Tel: +90 (212) 338-1362

† Electronic supplementary information (ESI) available. See DOI: https://doi.org/10.1039/d5ma00017c
‡ These authors contributed equally.

MOFs have not been widely studied: MIL-88 analogues were computationally constructed from larger dicarboxylic acid moieties to extend its pore size,[22] however, when the CO_2 capture capacity of MIL-88 analogues was computationally investigated, they were reported to underperform the parent MIL-88.[23] Benzene-1,4-dicarboxylic acid linker of MOF-5 and 2,5-dioxobenzene-1,4-dicarboxylate (DOBDC) linker of MOF-74 were replaced with various dicarboxylic acids to enhance their CH_4 and CO_2 uptakes.[24,25] Hypothetical MOFs with Zr nodes and different topologies were generated by combining linker-exchange and functionalization approaches and these MOFs achieve high CH_4 deliverable capacities.[26]

Lanthanide MOFs (Ln-MOFs, also known as lanthanide organic frameworks-LOFs) are multi-functional materials having remarkable structural diversity with interesting chemical and physical properties that enable them to be used in various applications such as luminescence sensing, catalysis, magnetism, gas storage, and separation applications.[27–32] Due to the high coordination numbers of Ln-metals and their flexible coordination environment, modification and construction of Ln-MOFs and the ease of solvent removal from their framework without any permanent pore collapse offer a promising space for the design and synthesis of new high-performing and stable Ln-MOFs for gas adsorption and separation.[33–36] However, CO_2/N_2 separation studies using Ln-MOFs are limited in the literature.

Experimental studies only focused on a few Ln-MOFs, which have relatively low CO_2/N_2 selectivities up to 19.2,[37] 22.4,[38] and 29.0[39] at 273 K. Large-scale computational screening studies revealed that Ln-MOFs with distinct structural properties are very promising for CO_2/N_2 separation among thousands of MOFs. For example, Qiao et al.[31] calculated the adsorption selectivity, working capacity, and regenerability of 4764 computation-ready experimental (CoRE) MOFs for CO_2/N_2 separation and results showed that 13 out of 15 top-performing MOFs contain Ln as the metal. CATART03, SEV-WEV, and MUFJAZ01 were identified as the most promising MOFs, which contain Ca, Nd, and Eu metals, respectively. Our group computed CO_2/N_2 selectivities and CO_2 permeabilities of 3806 MOFs obtained from the Cambridge Structural Database (CSD) and showed that three top-performing Ln-MOFs are NURVAZ, PEXSAO, and SAJFEO with La, Gd, and La metals, respectively.[40] The promising Ln-based MOFs for membrane-based CO_2/N_2 separation were found to possess narrow pores, low porosities, and low surface areas. As this literature review demonstrates, existing studies either focus on experimental measurement of the CO_2 adsorption and separation performance of a particular Ln-MOF or merely mention the importance of Ln-MOFs for CO_2/N_2 separation through computational screening of many MOFs. To better understand the potential of Ln-MOFs for CO_2 capture, studying these structures at the atomic-level and establishing useful structure–performance relationships based on molecular-insights is strongly required.

In this work, we used both atomic- and molecular-level calculations to tune the CO_2/N_2 separation performances of an Ln-MOF by linker- and metal-exchange methods. We first searched the CoRE MOF database to identify 2288 Ln-MOFs and then performed grand canonical Monte Carlo (GCMC) simulations to compute their CO_2/N_2 mixture adsorption and separation performance metrics such as selectivities, working capacities, adsorbent performance scores, and regenerabilities. One of the top-performing Ln-MOFs was selected as the genotype MOF for metal and linker exchange. The linkers of the selected Ln-MOF were exchanged with 5 different linkers and its metal atom was exchanged with 12 different Ln metals. In this way, we generated 77 different types of hypothetical Ln-MOFs, constructed from a total of 6 linkers and 13 Ln-metals, excluding the parent MOF. These structures were first optimized at the molecular mechanics (MM)-level, and then their CO_2/N_2 mixture adsorption and separation performances were studied by GCMC simulations. Computer-generated Ln-based MOFs, which outperformed the genotype Ln-MOF in terms of selectivity and adsorbent performance score, were identified and subjected to quantum mechanics (QM)-level optimizations. The relationships between the separation performance metrics of hypothetical Ln-MOFs and their physical and chemical properties were investigated in detail to understand which molecular features are critical to achieve high-performance CO_2 capture. The computational approach we described and followed in this study is expected to guide future studies for the rational design and discovery of novel functional materials with desirable gas separation properties.

2. Computational details

The computational protocol that we followed for the selection of a genotype Ln-MOF among 2288 Ln-MOFs and the modification of the genotype Ln-MOF with the aim of designing a superior hypothetical material for CO_2/N_2 separation is displayed in Fig. 1. We used the most recent computation-ready experimental, all-solvents-removed MOF database (CoRE MOF 2019 ASR), which contains 10 143 different types of non-disordered MOFs.[41] 2288 MOFs containing lanthanides (La^{3+}, Ce^{3+}, Pr^{3+}, Nd^{3+}, Sm^{3+}, Eu^{3+}, Gd^{3+}, Tb^{3+}, Dy^{3+}, Ho^{3+}, Er^{3+}, Tm^{3+}, Yb^{3+}, and Lu^{3+}) were initially selected from this database. Structural properties of these Ln-based MOFs, such as pore limiting diameter (PLD), the largest cavity diameter (LCD), N_2 accessible surface area (S_{acc}), and porosity (ϕ) were computed using Zeo++ software.[42] MOFs with nonzero gravimetric surface areas and PLDs greater than 3.64 Å were considered for further investigation to ensure that both CO_2 (3.30 Å) and N_2 (3.64 Å) molecules could be adsorbed into the pores of the adsorbents.

To compute the CO_2/N_2 mixture adsorption in Ln-MOFs, electrostatic interactions between the gas molecules and MOFs should be considered and hence the charge equilibration method (Q_{eq}), as implemented in the RASPA[43] simulation code, was used to assign partial point charges to Ln-MOF atoms.[44,45] Any MOF with a partial point charge larger than 5.0 or smaller than −5.0 was eliminated. The Ln-MOFs for which Henry's constant of CO_2 (K_{CO_2}) was computed to be higher than 10^{-2} mol kg^{-1} Pa^{-1} were not considered since the regenerability of a material with a very high Henry's constant might be
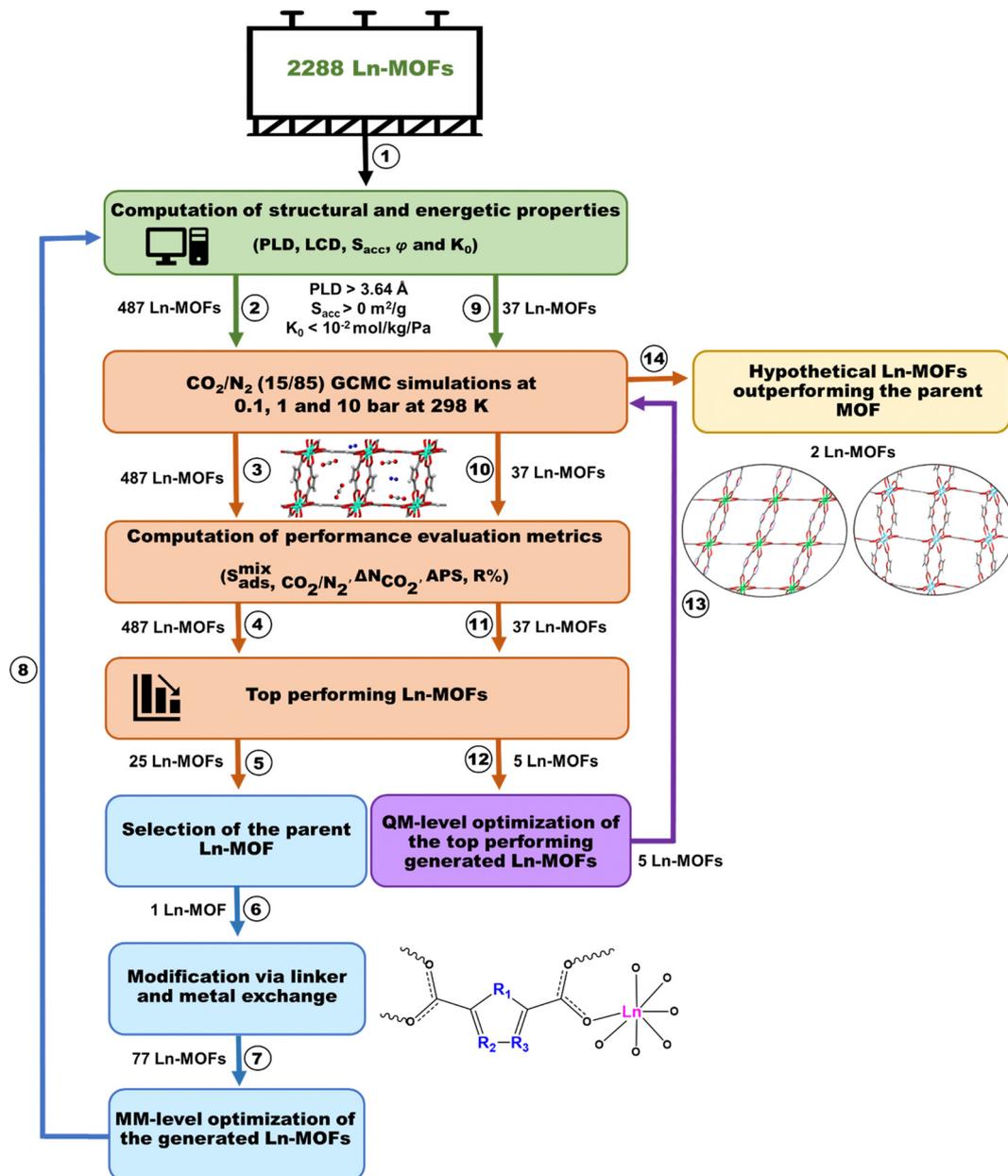
Fig. 1 Schematic representation of the computational workflow, together with the number of Ln-MOFs passed to the next level of calculations in each step.

challenging due to the presence of strong adsorbate–adsorbent interactions.[46,47] After these eliminations, 487 Ln-MOFs were found to be eligible for CO_2/N_2 separation application. Fig. S1 (ESI†) shows the distribution of metals in 487 Ln-MOFs evaluated in this study: Gd-MOFs exhibit the largest group (101 MOFs), whereas Tm-MOFs constitute the group with the lowest number of MOFs in the distribution (5 MOFs). There is no MOF constructed from Pm^{3+} metal in the CoRE MOF database, and Nd^{3+}-based MOFs were eliminated due to the filters described above.

GCMC simulations were performed using the RASPA[43] simulation code version 2.0.37 to obtain the CO_2/N_2 mixture adsorption data of 487 different types of Ln-MOFs. To represent

dry flue gas, we specified the composition of the CO_2/N_2 mixture as 15/85. The temperature was fixed to the ambient temperature (298 K). The Lennard-Jones (LJ) potential was used to compute the non-bonded interactions, and a cut-off distance of 13 Å was set for the truncation of these interactions. The simulation cell lengths were set to at least twice of the cut-off distance. The universal force field (UFF) was used for the potential parameters of MOF atoms.[48] Potential parameters for CO_2 molecule were taken from the TraPPE force field.[49] CO_2 was modeled as a three-site linear, rigid molecule with partial point charges located at the center of each site. For N_2 molecule, a three-site model was used with N atoms at the two sites, and the third site was the center of mass with

partial charges.[50] The Lorentz–Berthelot mixing rules were applied to obtain pair potentials between dissimilar atoms. The Ewald summation was used to consider the long-range electrostatic interactions.[51]

CO_2/N_2 mixture adsorption performances of 487 Ln-MOFs were calculated under vacuum swing adsorption (VSA) and pressure swing adsorption (PSA) process conditions, where adsorption (desorption) pressure was set to 1 (0.1) and 10 (1) bar, respectively, for VSA and PSA processes. GCMC simulations for CO_2/N_2 mixture were performed with 60 000 cycles (10 000 cycles for initialization, 50 000 cycles for taking ensemble averages). To further understand how cyclic adsorption processes affect the gas separation performances; mixture selectivities ($S_{ads,CO_2/N_2}$), working capacities (ΔN_{CO_2}), and adsorbent performance scores (APS) of MOFs were computed at each process condition using the formulas given in Table S1 (ESI†). The ratio of the composition of the adsorbed gases divided by the bulk composition of the mixture was used to calculate mixture adsorption selectivity. Working capacity was calculated as the difference of the CO_2 uptake computed at the adsorption and desorption pressures. APS was calculated as the multiplication of selectivity and working capacity. The isosteric heat of adsorption values for CO_2 and N_2 $\left(Q_{st}^{CO_2} \text{ and } Q_{st}^{N_2}\right)$ were obtained from the mixture GCMC simulations conducted at 1 bar and 10 bar. K_{CO_2} and K_{N_2} were calculated using the Widom particle insertion method[52] at infinite dilution with a total of 60 000 cycles where 10 000 cycles were used for the initialization.

487 Ln-MOFs were then ranked with respect to their calculated APSs under VSA condition, and one of the top-performing Ln-MOFs, YUSWIU, was selected as the genotype MOF. Original metal and linker atoms of this selected Ln-MOF, Dy^{3+} and furan-2,5-dicarboxylate, respectively, were exchanged using the "edit structure" tool implemented in Mercury software.[53] 77 hypothetical Ln-MOFs were generated. Since QM level optimizations of this large number of structures are computationally very demanding and time consuming, initial geometry optimizations of these structures were performed by using the Forcite module of Materials Studio[54] with the aim to relax all atomic coordinates and cell parameters for an efficient pre-screening of the generated Ln-MOFs. The convergence tolerance quality of ultra-fine (energy tolerance value of 2×10^{-5} kcal mol^{-1}, displacement tolerance value of 10^{-5} Å, and force tolerance value of 10^{-3} kcal) and smart algorithm, which uses the steepest descent, adjusted basis set Newton-Raphson and quasi-Newton methods to find the lowest energy conformation with maximum iteration numbers of 10 000 were employed, and the cell parameters were allowed to be optimized. The potential parameters were taken from the UFF for MOFs, and the partial point charges were assigned by the Q_{eq} method, which offers an affordable computational cost with high accuracy. After this initial geometry optimization at the MM-level, 37 hypothetical Ln-MOFs were identified to meet the eligibility requirements discussed above (PLD > 3.64 Å, S_{acc} > 0 m^2 g^{-1}, $K_0 < 10^{-2}$ mol kg^{-1} Pa^{-1}). GCMC simulations were performed to assess their CO_2/N_2 mixture adsorption and separation performances, and they were ranked with respect to their selectivities and APSs computed under VSA and PSA conditions. Five of them were identified to outperform the parent Ln-MOF both in VSA and PSA conditions.

To obtain MOF geometries closer to expected real structures, these five hypothetical Ln-MOFs were further subjected to geometry optimizations at the QM-level. QM-level optimizations of the one-unit cell of the Ln-MOFs were conducted by the DMol3 module[55,56] implemented in the Materials Studio program package. With the aim of testing the capability of the most commonly employed density functional theory (DFT) methodologies for reproducing the experimental structural properties, the generalized gradient approximation (GGA) Perdew–Burke–Ernzerhof (PBE) functional,[57] hybrid-GGA exchange–correlation Becke-3-parameter-Lee–Yang–Parr (B3LYP) functional[58,59] together with double numerical plus d-function (DND) and double numerical plus polarization function (DNP) basis sets were used. A spin-unrestricted formalism was employed for the treatment of spin polarization. The Monkhorst–Pack scheme k-points grid sampling was set as $1 \times 3 \times 1$. The convergence tolerance quality of fine (energy tolerance value of 10^{-5} Ha, displacement tolerance value of 5×10^{-5} Å, force tolerance value of 2×10^{-3} Ha Å^{-1}, and SCF tolerance value of 10^{-6}) was set, in which the cell parameters were allowed to be optimized. GCMC simulations were then performed to assess the CO_2/N_2 separation performance of QM-level optimized Ln-MOFs. In these simulations, partial atomic charges in metal–organic frameworks (PACMOF)[60] charges which are based on the density derived electrostatic and chemical (DDEC) charges[61] were assigned to QM-optimized Ln-MOF structures for the highest accuracy.

3. Results and discussions

Identification of the MOF genotype with desired properties is the principal step in materials design which is followed by the modification of its organic linkers and inorganic nodes. While linker replacement provides the freedom for the incorporation of chemical moieties of interest, metal exchange expands the structural and compositional diversity of a material. With the aim of finding the most suitable MOF as the genotype, adsorption-based CO_2/N_2 separation performances of 487 Ln-MOFs were initially examined to find the top-performing materials offering high $S_{ads,CO_2/N_2}$ and ΔN_{CO_2} with a high $R\%$.

Fig. 2(a) and (b) show the simulated $S_{ads,CO_2/N_2}$ and ΔN_{CO_2} values of 487 Ln-MOFs computed at VSA and PSA conditions. At VSA (PSA) condition, $S_{ads,CO_2/N_2}$ and ΔN_{CO_2} values varied between 3–15 508 and 0.03–3.9 mol kg^{-1} (3–19 284 and 0.03–8.1 mol kg^{-1}), respectively. For an efficient and cost-effective gas separation process, an adsorbent should have both a high working capacity and a high selectivity. APS, which is the multiplication of adsorption selectivity and working capacity, was employed to evaluate the performance of Ln-MOFs for CO_2/N_2 separation. Ln-MOFs that are represented with blue and red
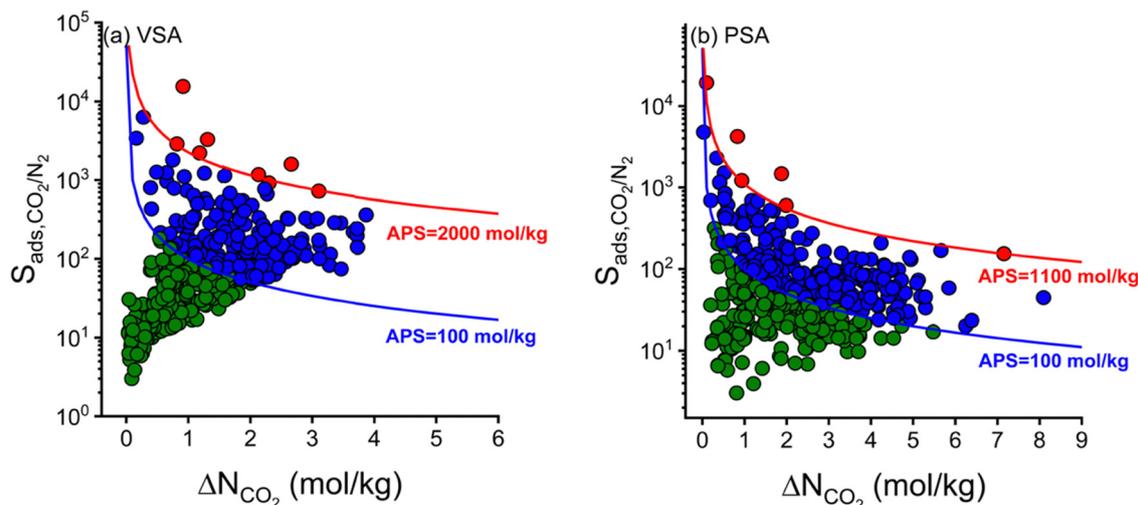
Fig. 2 Simulated $S_{ads,CO_2/N_2}$ and ΔN_{CO_2} values for 487 Ln-MOFs for CO_2/N_2 separation at (a) VSA and (b) PSA conditions. Green, blue, and red points represent MOFs with (a) APS < 100 mol kg^{-1}, 100 < APS < 2000 mol kg^{-1}, and APS > 2000 mol kg^{-1}, respectively, (b) APS < 100 mol kg^{-1}, 100 < APS < 1100 mol kg^{-1}, and APS > 1100 mol kg^{-1}, respectively.

points in Fig. 2 correspond to materials offering moderate and high APSs, respectively. Under VSA condition, 11 Ln-MOFs out of 487 have moderate to high APSs (553–14 193 mol kg^{-1}) because of their very high $S_{ads,CO_2/N_2}$ (734–15 508), although they have considerably low ΔN_{CO_2} (< 1 mol kg^{-1}), as shown in Fig. 2(a). 10 Ln-MOFs with moderate $S_{ads,CO_2/N_2}$ (140–362) and high ΔN_{CO_2} (> 3 mol kg^{-1}) also achieve a range of moderately high APSs (452–1400 mol kg^{-1}). Similarly, at PSA condition, Ln-MOFs with very high $S_{ads,CO_2/N_2}$ (1136–19 234) and low ΔN_{CO_2} (< 1 mol kg^{-1}) have moderate to high APSs (141–3513 mol kg^{-1}) and Ln-MOFs with moderate $S_{ads,CO_2/N_2}$ (108–208) and high ΔN_{CO_2} (>3 mol kg^{-1}) have APSs in the range of 426–1100 mol kg^{-1}, as shown in Fig. 2(b). Since the VSA process yielded higher APSs compared to the PSA process, the top promising 25 Ln-MOFs were identified for CO_2/N_2 separation, considering the highest APS for the VSA process with R% > 75%. All calculated adsorbent performance metrics of the top 25 Ln-MOFs, together with their structural properties, were listed in Table S2 (ESI†) and results show that the top Ln-MOFs having R% > 75% also have moderate APSs (145–843 mol kg^{-1}) and $S_{ads,CO_2/N_2}$ (73–325).

The top 25 Ln-MOFs are mainly composed of benzene- and pyridine-derived organic linkers, three of them have cyclohexane (COWMIL, KULRIT, and COWMAR), one contains oxalato (OJO-NOQ), and two have furan scaffolds (YUSWIU and QUZVEO). Linkers connected to the inorganic nodes of Ln-MOFs through carboxylate fragments were reported to implement porous and robust character to the framework.[33,35] Besides, rigid and linear ligands preserve the rigidity and topological network of the crystal structure. Among the top performing 25 Ln-MOFs listed in Table S2 (ESI†), modification of YUSWIU, which offers moderate APSs (146 and 200 mol kg^{-1} at VSA and PSA conditions), was interesting since furan-2,5-dicarboxylate linkers can be replaced with various rigid and commercially available 5-membered heterocyclic-dicarboxylic acids. Therefore, we focused on both the linker and metal-exchange of the MOF named YUSWIU.

Dy^{3+} atoms in YUSWIU bond to six carboxylate O atoms of furan-2,5-dicarboxylic acid, one O atom is coordinated to dimethylformamide (DMF) solvent, and one O atom is coordinated to methanol solvent.[60] Four carboxylate groups bridge the two Dy^{3+} centers. The furan-2,5-dicarboxylate linkers of YUSWIU were replaced with 5 different types of linkers which are: pyrrole-2,5-dicarboxylate (hereafter denoted as Ln-pyrrole), 4-amino-1,2,4-triazole-3,5-dicarboxylate (Ln-aminetriazole), 4-methyl-1,2,4-triazole-3,5-dicarboxylate (Ln-methyltriazole), isoindoline-1,3-dicarboxylate (Ln-isoindoline) and 1,3,4-oxadiazole-2,5-dicarboxylate (Ln-oxadiazole). Then, Dy^{3+} metal of every linker-exchanged YUSWIU structure and the original YUSWIU were replaced with 12 Ln-metals; La^{3+}, Ce^{3+}, Pr^{3+}, Sm^{3+}, Eu^{3+}, Gd^{3+}, Tb^{3+}, Ho^{3+}, Er^{3+}, Tm^{3+}, Yb^{3+}, Lu^{3+} to generate a total of 77 YUSWIU-derived Ln-MOFs as shown in Fig. 3.

Initial conformations of all generated structures were subjected to periodic geometry optimizations at the MM-level with the Forcite module of the Materials Studio program package to attain a MOF geometry with minimized total energy. Although generic force fields such as UFF may have limitations in the representation of interactions, optimizations at the MM-level were shown to perform well in predicting the geometric parameters for MOFs.[18] We note that lanthanides have unique electronic properties, and UFF parameterization might not capture them well. In this study, UFF-based optimization was used for pre-screening the materials before the computationally demanding QM-level optimizations. To test the reliability of our method, the crystal structure of YUSWIU was optimized with the parameters described in the methodology section. The Dy–O and Dy–Dy bond lengths of YUSWIU were reported to be 2.256–2.594 Å (shortest–longest) and 4.122 Å, respectively.[62] The corresponding bond distances in the optimized YUSWIU were observed to be fairly close to the reported values (r_{Dy-O} = 2.220–2.388 Å, r_{Dy-Dy} = 4.317 Å). The unit cell parameters of the optimized YUSWIU deviated from the experimental data by less
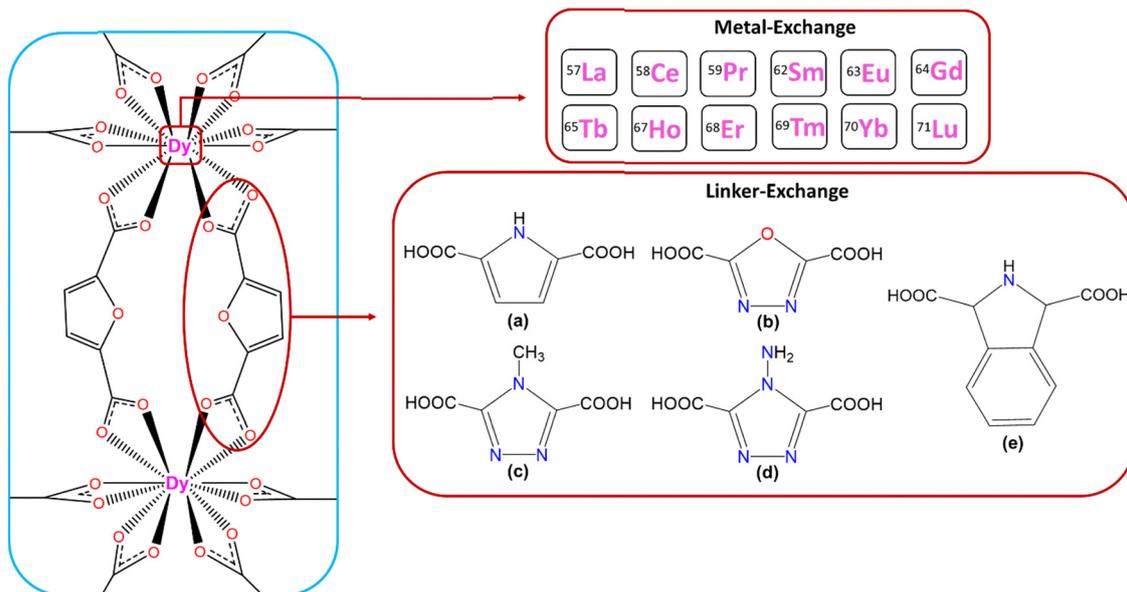
Fig. 3 Proposed linkers and Ln metals to be exchanged with the linker and metal atom of the genotype Ln-MOF, YUSWIU. (a) Pyrrole-2,5-dicarboxylic acid, (b) 1,3,4-oxadiazole-2,5-dicarboxylic acid, (c) 4-methyl-1,2,4-triazole-3,5-dicarboxylic acid, (d) 4-amino-1,2,4-triazole-3,5-dicarboxylic acid, (e) isoindoline-1,3-dicarboxylic acid.

than 4.7%, which gives an acceptable degree of confidence in terms of the quality of the geometry for the initial screening of the generated Ln-MOFs.

When the Dy^{3+} atoms of YUSWIU (Dy-furan) were exchanged with 12 Ln-metals, optimized Ln–Ln distances decreased gradually from $^{57}La^{3+}$ (4.606 Å) to $^{71}Lu^{3+}$ (2.701 Å) in accordance with the lanthanide contraction concept; the atomic radius of lanthanide elements decreases as the atomic number increases,[63] with only exceptions in Eu–Eu (4.508 Å) and Yb–Yb (4.946 Å) distances, as given in Table S3 (ESI†). Eu has an electronic configuration of [Xe] $6s^2$ $4f^6$ (half-filled f subshell), and Yb has an electronic configuration of [Xe] $6s^2$ $4f^{14}$ (full-filled f subshell), and thus they can access +2 oxidation state instead of +3 which makes them relatively more stable. Eu and Yb have larger metallic radii compared to other trivalent Ln-metals, consistent with the divalent nature of these two Ln-metals. As a result, they behave exceptionally in the Ln–Ln bond length trend. Ln–O bond lengths also show a rough decrease from $^{57}La^{3+}$ to $^{71}Lu^{3+}$ as observed in Ln–Ln distances, with large deviations in Eu–O and Yb–O bonds. When the furan ring in YUSWIU (Dy-furan) was exchanged with 5-membered heterocycles, Dy–Dy and the shortest Dy–O distances were observed to be slightly longer in Dy-aminetriazole, Dy-oxadiazole, and Dy-methyltriazole than YUSWIU, whereas Dy–Dy and the largest Dy–O bond lengths were calculated to be slightly shorter in Dy-pyrrole and Dy-isoindoline, as in Table S4 (ESI†).

After the geometry optimizations of YUSWIU-derived MOFs, their structural properties (PLD, LCD, S_{acc}, ϕ) were computed. 40 generated Ln-MOFs were eliminated due to the previously applied filters such that if an Ln-MOF has PLD < 3.64 Å or $K_{CO_2} > 10^{-2}$ mol kg^{-1} Pa^{-1}. As a general trend, none of the Ln-MOFs constructed from isoindoline-1,3-dicarboxylate (Ln-isoindoline)

and 4-methyl-1,2,4-triazole-3,5-dicarboxylate (Ln-methyltriazole) could give PLD > 3.64 Å because of the steric effects caused by the large molecular volumes of these moieties. Thus, we ended up with 37 YUSWIU-derived structures. Table S5 (ESI†) represents the structural properties of these 37 Ln-MOFs, having pore sizes of 4.87 Å ≤ LCD ≤ 6.41 Å and 3.74 Å ≤ PLD ≤ 5.74 Å. MOFs generated from 4-amino-1,2,4-triazole-3,5-dicarboxylate linkers (Ln-aminetriazole) have the lowest S_{acc}, varying between 125–559 m^2 g^{-1}, whereas the MOFs generated from furan-2,5-dicarboxylate linkers (Ln-furan) generally have the highest S_{acc}, varying between 1043–1332 m^2 g^{-1} (excluding Lu-furan), followed by Ln-pyrroles and Ln-oxadiazoles, in accordance with the molecular volumes of the linkers. On the other hand, when the metal atoms are considered, calculated S_{acc} values generally decreased with the increased atomic size of the Ln-metal; Lu-MOFs have the lowest S_{acc}, varying between 323–431 m^2 g^{-1} and Yb- and La-MOFs have the largest S_{acc}, varying between 1074–1332 m^2 g^{-1}, excluding aminetriazoles.

Fig. 4 shows the $S_{ads,CO_2/N_2}$ and ΔN_{CO_2} values computed from the results of molecular simulations of 37 hypothetical Ln-MOFs that we generated by linker and metal-exchange, together with 487 synthesized Ln-MOFs for which the $S_{ads,CO_2/N_2}$ and ΔN_{CO_2} results were previously presented in Fig. 2. As a general trend, $S_{ads,CO_2/N_2}$ and ΔN_{CO_2} values of hypothetical YUSWIU analogues are cumulated amid the $S_{ads,CO_2/N_2}$ and ΔN_{CO_2} values of the synthesized Ln-MOFs. Under VSA condition, the range of $S_{ads,CO_2/N_2}$ and ΔN_{CO_2} for hypothetical YUSWIU-derived MOFs were computed as 16–595 and 0.5–2.4 mol kg^{-1}, respectively. Among 37 YUSWIU derived-MOFs, 8 of them have higher $S_{ads,CO_2/N_2}$ (117–595) and APS (236–1023 mol kg^{-1}) than YUSWIU (80 and 146 mol kg^{-1}, respectively) at VSA process. The range of $S_{ads,CO_2/N_2}$ and ΔN_{CO_2} values for YUSWIU-derived MOFs
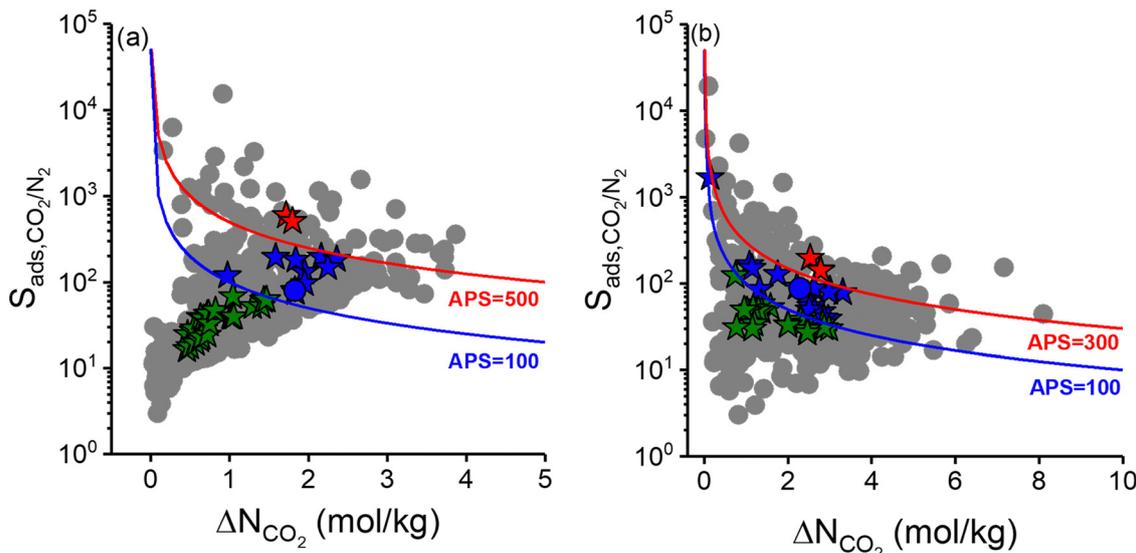
Fig. 4 Simulated $S_{ads,CO_2/N_2}$ and ΔN_{CO_2} for 37 different types of computer-generated YUSWIU-derived MOFs for CO_2/N_2 separation at (a) VSA and (b) PSA conditions. Blue circle represents the performance of YUSWIU. Green, blue, and red points represent the YUSWIU-derived MOFs with (a) APS < 100 mol kg^{-1}, 100 < APS < 5000 mol kg^{-1}, and APS > 500 mol kg^{-1}, respectively, (b) APS < 100 mol kg^{-1}, 100 < APS < 300 mol kg^{-1}, and APS > 300 mol kg^{-1}, respectively. Simulated data for 487 synthesized Ln-MOFs were shown by grey in the back for comparison.

under PSA condition were computed between 27–198 and 0.7–3.3 mol kg^{-1}, respectively. Six YUSWIU-analogues were identified to have higher $S_{ads,CO_2/N_2}$ (91–198) and APS (202–500 mol kg^{-1}) than the parent Ln-MOF (88 and 200 mol kg^{-1}, respectively), whereas three of them have higher APS (237–260 mol kg^{-1}) but slightly lower $S_{ads,CO_2/N_2}$ (79–84 mol kg^{-1}) at PSA process.

Fig. 4 also shows interesting trends in the MOFs generated from Ln metals. For instance, Ln-aminetriazoles were calculated to have low porosities (0.46–0.52) and low S_{acc} (125–559 m^2 g^{-1}), which limits their gas uptakes and APSs. On the other hand, no hypothetic Ln-MOF with Dy, Er, Gd, Ho, Lu, Tb or Yb metal could outperform YUSWIU in terms of selectivity and APS. We observed a linear trend between the Q_{eq} charges assigned to Ln-metals and their CO_2 uptakes at 1 bar, when MOFs have similar porosities. 19 out of 37 Ln-MOFs listed in Table S5 (ESI†) have porosities between 0.57–0.59 and Ln-MOFs with more positively charged lanthanides appear to have stronger CO_2 uptake, as depicted in Fig. S2 (ESI†). While partial charges for Dy, Er, Gd, Ho, Tb, and Yb are scattered between 1.16–1.87e, partial charges of Ce, Eu, La, Lu, Pr, Sm, and Tm span a wide range between 2.11–3.93e. Although Lu metal has a partial positive charge of ∼2.65e, the narrow porosity of Lu-furan and Lu-pyrrole (0.49) permits less CO_2 uptake than Ln-MOFs with higher Ln charges, but higher uptake than those with lower charges. Since lanthanides are electropositive elements, electrons of the Ln metals are withdrawn by the electronegative coordinating oxygens of the linkers. We also observed that carboxylate oxygens of Ce, Eu, La, Lu, Pr, Sm, and Tm-MOFs are more negatively charged compared to the carboxylate oxygens of Dy, Er, Gd, Ho, Tb, and Yb-MOFs, and the more electron-rich oxygens attract Lewis acidic (electron acceptor) CO_2 stronger. Further examination of 19 Ln-MOFs having

similar porosities for the effect of linker type on CO_2 uptake reveals that oxadiazole linkers almost double the CO_2 uptake compared to furan, which adsorbs CO_2 stronger than pyrrole at 1 bar. Furan and pyrrole-based linkers were observed to adsorb N_2 strongly compared to oxadiazole-based linkers. Oxadiazole linkers were previously shown to have high CO_2/N_2 selectivity due to the presence of two nitrogen atoms (bearing lone pairs) in its heterocyclic ring, which attract CO_2.[64] Five YUSWIU derived-MOFs common in VSA and PSA conditions were identified to outperform the original YUSWIU structure in terms of selectivity and APS. Their calculated properties are given in Table S6 (ESI†).

In the next step, these promising five materials identified to have higher selectivity and APS than the original YUSWIU structure were considered for the computationally more demanding QM-level geometry optimizations. For the benchmarking study of the DFT method, PBE/DNP, PBE/DND, and B3LYP/DNP level theories were tested. The crystal structure of YUSWIU was subjected to geometry optimizations by employing the three DFT functional and basis set combinations. When the geometrical parameters including the bond lengths and unit cell parameters of the crystal structure of YUSWIU were compared with the three optimized geometries, B3LYP/DNP was found to give markedly longer Dy–O and Dy–Dy bonds (5–7%) and larger cell volume (20.9%), whereas the corresponding deviations were smaller than 2.9% in bond lengths and 7.4% larger in cell volume when YUSWIU was optimized with PBE/DND. On the other hand, when PBE/DNP level of theory was used, the largest and the shortest Dy–O bonds of optimized YUSWIU (2.779 Å and 2.454 Å) were slightly overestimated and underestimated, respectively, compared to the original crystal structure (2.256 and 2.594 Å), and Dy–Dy bond (4.092 Å) was slightly underestimated with respect to the crystal

structure (4.122 Å), whereas the unit cell parameters and cell volume deviate from the experimental data by less than 2.7% and 5.3%, respectively. Besides, geometry optimization at the PBE/DNP level resulted in closer unit cell parameters compared to the MM-level optimization (less than 2.7% deviation for QM and less than 4.7% deviation for MM-level optimized YUSWIU). Thus, five promising hypothetical Ln-MOFs were further optimized by using the PBE/DNP level of theory. Calculated structural properties, LCD, PLD, S_{acc}, and ϕ of QM-level optimized Ln-MOFs presented in Table S7 (ESI†) were observed to be different from the calculated properties for their MM-optimized geometries. MOFs containing furan linkers (La-furan and Tm-furan) were computed to have slightly lower LCD and PLDs (less than 0.12 Å) in QM-level optimized structures, whereas higher LCD and PLDs were computed for QM-level optimized structures of YUSWIU-derived MOFs with oxadiazole (Pr-oxadiazole, Sm-oxadiazole and Tm-oxadiazole) linkers (between 0.37–0.97 Å) compared to their MM-optimized counterparts. These changes are considered within the acceptable limits according to a previous computational study, where 90% of 879 MOFs experienced changes in their LCDs less than 1 Å upon QM-level geometry optimization.[65]

Adsorbent performance metrics were computed from scratch for the QM-level optimized YUSWIU analogues by assigning PACMOF charges. To ensure consistency of the performance comparisons between YUSWIU and its hypothetic analogues, PACMOF charges were also assigned to YUSWIU. Comparisons of the simulated N_{CO_2} and $S_{ads,CO_2/N_2}$ values of MM- and QM-level optimized Ln-MOFs are shown in Fig. 5. The calculated metrics for YUSWIU and five hypothetic YUSWIU-derived MOFs were found to be different when two different methodologies (MM-level optimization with Q_{eq} charges vs. QM-level optimization with PACMOF charges) were used. MM-level optimized and Q_{eq} charge-assigned hypothetical Ln-MOFs exhibit equal or higher CO$_2$ uptake at 1 bar than QM-level optimized and PACMOF charge-assigned counterparts (Fig. 5(a)), whereas the reverse trend is observed at 10 bar (Fig. 5(b)) and for YUSWIU at 1 bar and 10 bar. For N$_2$ uptakes, while similar trends are observed for hypothetical Ln-MOFs, YUSWIU presents a reverse trend (Fig. S3, ESI†). Nazarian et al.[65] showed that the CO$_2$ uptake of 82% of 879 MOFs changed more than 5% after the geometry optimization, indicating that gas adsorption properties can differ depending on the free energy landscape of the MOFs. Thus, the changes in geometrical parameters upon optimization at the QM-level result in different CO$_2$ and N$_2$ uptakes. On the other hand, when we considered the charge effect, CO$_2$ uptake of PACMOF-charged YUSWIU at 1 bar was computed to be 17% more than the Q_{eq}-charged YUSWIU (Fig. 5(a)), while at 10 bar, the assigned charges have little impact on the CO$_2$ uptake as expected due to the decreased impact of adsorbate–adsorbent interactions (Fig. 5(b)).

At 1 bar, Pr-oxadiazole, Sm-oxadiazole, Tm-oxadiazole and La-furan were calculated to possess higher CO$_2$ uptakes (Fig. 5(a)), whereas five hypothetic Ln-MOFs have lower N$_2$ uptakes than YUSWIU (Fig. S3, ESI†) which results in higher $S_{ads,CO_2/N_2}$ for Pr-oxadiazole, Sm-oxadiazole, Tm-oxadiazole, and La-furan

compared to YUSWIU when the two methodologies were considered (Fig. 5(b)). However, at 10 bar, although all the hypothetical Ln-MOFs have higher CO$_2$ uptakes than YUSWIU (Fig. 5(c)), only Tm-oxadiazole exhibits a higher CO$_2$ selectivity assessed by both methodologies (Fig. 5(d)), because of the increased N$_2$ uptakes in Pr-oxadiazole, Sm-oxadiazole, La-furan and Tm-furan (Fig. S3, ESI†). We observed a large gap between the calculated $S_{ads,CO_2/N_2}$ of MM- and QM-level optimized Pr-oxadiazole at 10 bar which is due to the drastically higher N$_2$ uptake calculated for the QM-level optimized, PACMOF-charged structure than the MM-level optimized, Q_{eq}-charged structure (Fig. S3, ESI†).

With the aim to see how the gas uptakes change with our proposed methodology, we tested the combined effect of charge and the optimization method on the gas uptakes by performing the simulations on the MM-level optimized, Q_{eq} charge-assigned YUSWIU and the QM-level optimized, PACMOF charge-assigned YUSWIU. Results showed that CO$_2$ uptake of the QM-level optimized, PACMOF charge-assigned YUSWIU at 1 (10) bar is 12% (7%) higher than the MM-level optimized, Q_{eq} charge-assigned YUSWIU. While charge alone did not have a significant impact on N$_2$ uptake (Fig. S3, ESI†), MM-level optimized, Q_{eq} charge-assigned YUSWIU have ∼30% higher N$_2$ uptakes than QM-level optimized, PACMOF charge-assigned YUSWIU at 1 bar and 10 bar. These results point out the importance of the choice of the methodology to be applied in the computational design of materials.

Table S8 (ESI†) shows the comparison between the highest positive and the lowest negative charges when Q_{eq} and PACMOF charges were assigned to the QM- and MM-level optimized geometries of five promising structures. For some MOFs, notable differences were observed, particularly for the metal centers. For instance, in Tm-furan, the highest positive charge for the QM-level optimized geometry is +2.10 (Q_{eq}) vs. 1.73 (PACMOF) for Tm atom, while the lowest negative charge is −0.47 (Q_{eq}) vs. −0.70 (PACMOF) for O atom, which resulted in higher K_{CO_2} for the PACMOF charge-assigned QM-level optimized geometry (1.4 × 10^{-4} mol kg^{-1} Pa^{-1}) than the Q_{eq} charge-assigned one (6.2 × 10^{-5} mol kg^{-1} Pa^{-1}). In the case of the MM-level optimized geometry of Pr-oxadiazole, the highest positive charge for the Q_{eq} charge-assigned structure (+3.87) is higher than the PACMOF charge-assigned one (+2.28), which resulted in higher K_{CO_2} (4.0 × 10^{-4} for Q_{eq} charges and 4.6 × 10^{-5} mol kg^{-1} Pa^{-1} for PACMOF charges). Despite these variations, we observed that the differences between the selectivities obtained from the ratio of Henry's constants of gases (K_{CO_2}/K_{N_2}) remained within an order of magnitude across different charge schemes, supporting the applicability of the Q_{eq} method for high-throughput screening while acknowledging its limitations in the selectivity predictions.

To gain deeper insights into the adsorption dynamics of the Ln-MOFs, CO$_2$/N$_2$ mixture adsorption snapshots in YUSWIU and five promising hypothetical Ln-MOFs (Pr-oxadiazole, Sm-oxadiazole, Tm-oxadiazole, La-furan, and Tm-furan) were generated. Fig. 6 shows that CO$_2$ and N$_2$ are gathered primarily around the carboxylate oxygens (red) in all Ln-MOFs. While CO$_2$
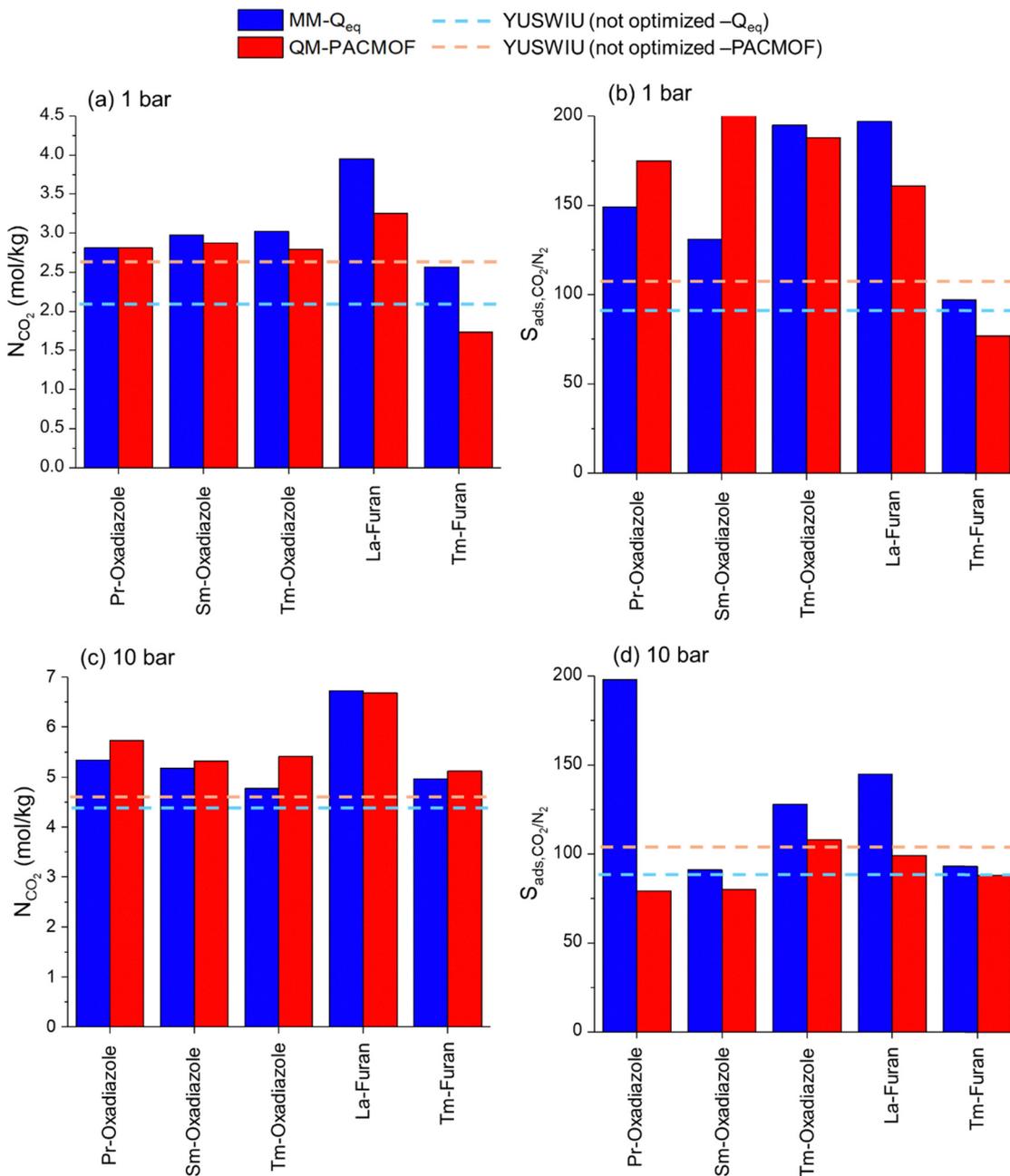
Fig. 5 Calculated CO_2 uptakes and $S_{ads,CO_2/N_2}$ at 1 bar (a) and (b), and at 10 bar (c) and (d) for original YUSWIU and YUSWIU-derived hypothetical MOFs.

is also cumulated around furan and oxadiazole rings, N_2 is only attracted by the furan ring since ring oxygens are weakly attractive for N_2, while nitrogen sites in oxadiazole repel N_2 molecules, decreasing their uptakes by the MOF. This behavior of N_2 molecules can be quantified by the isosteric heat of adsorption (Q_{st}) values, which shows the strength of the interactions between an adsorbate and an adsorbent. According to the Q_{st} values calculated at 1 bar (Table S9, ESI†), Pr-oxadiazole, Sm-oxadiazole, Tm-oxadiazole, La-furan, Tm-furan, and YUSWIU have a very high affinity for CO_2 $\left(Q_{st}^{CO_2} = 32.35{-}36.27 \text{ kJ mol}^{-1}\right)$ and moderate affinity for N_2

$\left(Q_{st}^{N_2} = 13.32{-}16.86 \text{ kJ mol}^{-1}\right)$. As a general trend, Ln-MOFs constructed from furan rings (Ln-furans) display slightly higher affinity for N_2, whereas Ln-oxadiazoles present a slightly lower affinity. On the other hand, we observe that Tm-oxadiazole has a much higher affinity for CO_2 (36.27 kJ mol^{-1}) than Tm-furan (32.64 kJ mol^{-1}), for which the node atoms are the same, but the linkers are different. These results indicate that 1,3,4-oxadiazole-2,5-dicarboxylate linkers dramatically increase the affinity for CO_2 and decrease the affinity for N_2 when replaced with furan-2,5-dicarboxylate leading to increased CO_2 selectivity. Both 1,3,4-oxadiazole and furan are aromatic
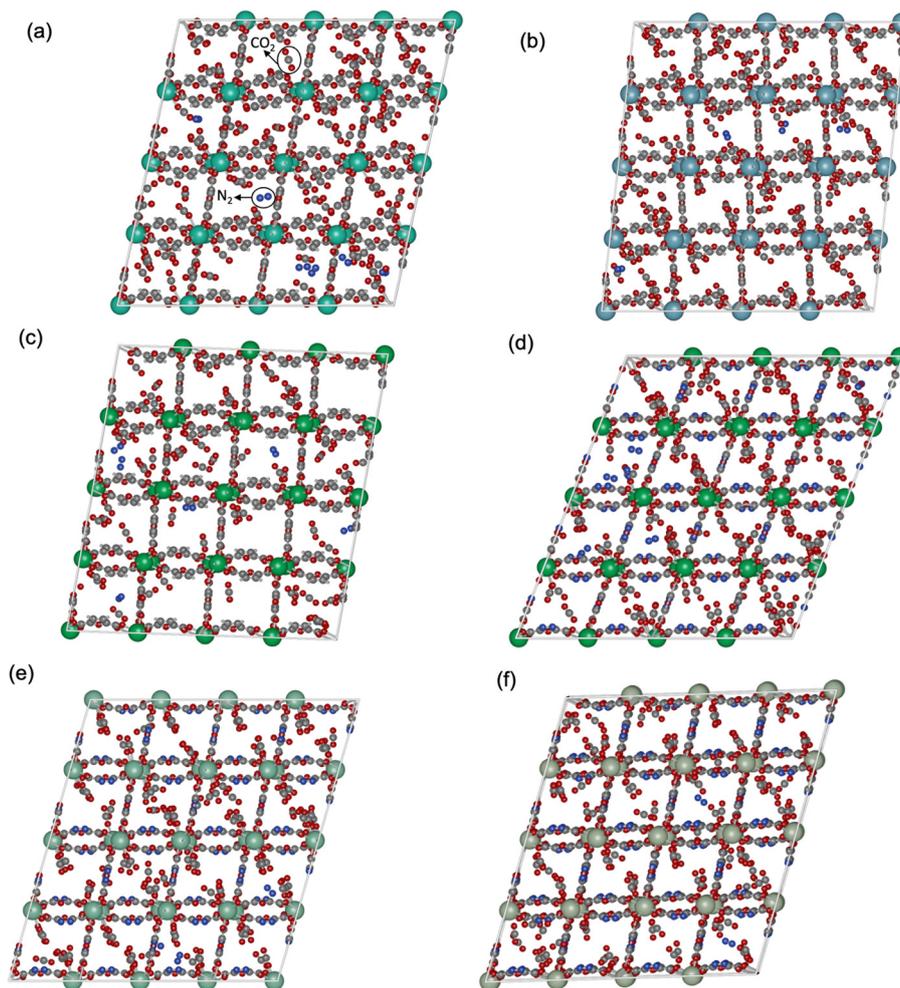
Fig. 6 Snapshots for CO_2 and N_2 adsorption in (a) YUSWIU (Dy-furan), (b) La-furan, (c) Tm-furan, (d) Tm-oxadiazole, (e) Sm-oxadiazole, and (f) Pr-oxadiazole at 1 bar, 298 K. Dy, La, Tm, Sm, C, O, H and N atoms are represented with cyan, light blue, dark green, light green, gray, red, white and dark blue, respectively.

rings, the latter more than the former. According to the previous DFT calculations, lone pair electrons on the oxygen and nitrogen atoms of the linker rings, which act as Lewis bases (electron-donor), are very good CO_2 adsorption sites that act as Lewis acid (electron-acceptor).[66,67] N_2, as a weak Lewis base, is also bound to oxygen sites, but more weakly compared to CO_2.

Selectivity is an interplay between various properties such as pore size, inorganic node, and linker type of the adsorbent, adsorbate polarizability and its affinity for the adsorbent. Higher CO_2 uptake and lower N_2 uptake in Tm-oxadiazole, thus higher $S_{ads,CO_2/N_2}$ compared Tm-furan, can be both attributed to the linker affinities for CO_2 and N_2, and to the larger pores of Tm-oxadiazole where more gas molecules can penetrate. On the other hand, although exchanging the Dy^{3+} nodes in YUSWIU (Dy-furan) with La^{3+} (La-furan) decreases the affinity of CO_2 ($Q_{st}^{CO_2} = 36.00$ kJ mol^{-1} for YUSWIU and 32.68 kJ mol^{-1} for La-furan) and N_2 ($Q_{st}^{N_2} = 16.86$ kJ mol^{-1} for YUSWIU and 14.47 kJ mol^{-1} for La-furan), larger porosity of La-furan allows higher CO_2 uptake, while N_2 uptake is slightly lower.

These findings pointed out the significance of furan-2,5-dicarboxylic acid and 1,3,4-oxadiazole-2,5-dicarboxylic acid in CO_2/N_2 separation performance of the material when incorporated into the MOFs as linkers and using Ln-metals as nodes which have electropositive character, willing to donate their electrons to coordinating oxygens, which in turn becomes more attractive for CO_2.

At 10 bar, the CO_2 affinities of YUSWIU, Pr-oxadiazole, Sm-oxadiazole, and Tm-oxadiazole were slightly lower ($Q_{st}^{CO_2} = 35.03, 31.90, 30.68$ and 34.57 kJ mol^{-1}, respectively), whereas La-furan and Tm-furan had slightly higher CO_2 affinities ($Q_{st}^{CO_2} = 33.66$ and 33.01 kJ mol^{-1}, respectively) compared to their corresponding values at 1 bar (Table S9, ESI†). In addition, the N_2 affinities of all Ln-MOFs were calculated to be profoundly higher $\left(Q_{st}^{N_2} = 15.94–17.99 \text{ kJ mol}^{-1}\right)$, resulted in lower CO_2 selectivities at 10 bar ($S_{ads,CO_2/N_2}$ varying between 79 and 108).

The comparison of APS values of these five promising QM-optimized Ln-MOFs (Pr-oxadiazole, Sm-oxadiazole, Tm-oxadiazole,
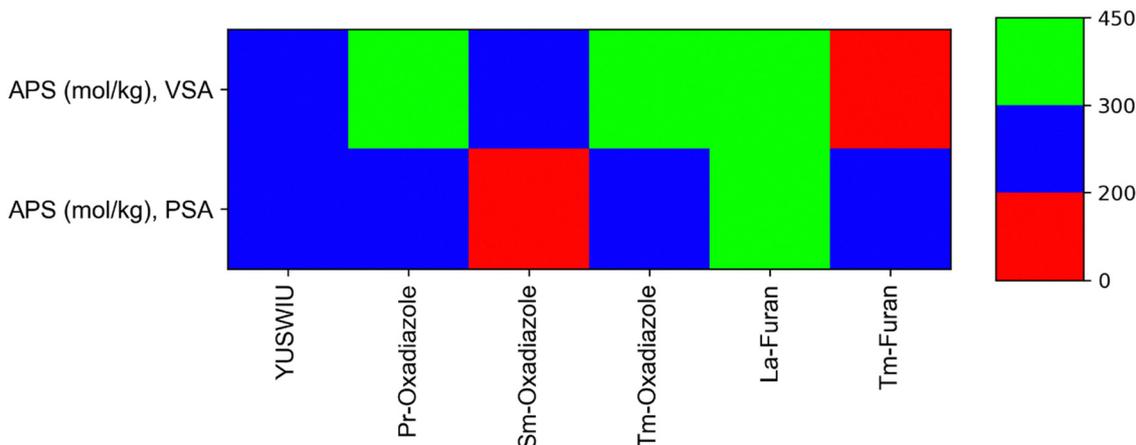
Fig. 7 APS of promising Ln-MOF candidates at VSA and PSA conditions. Geometries were optimized at QM-level and PACMOF charges were assigned. Data provided for YUSWIU were taken from the calculations performed for the PACMOF-assigned crystal structure.

La-furan, Tm-furan) and YUSWIU is presented in Fig. 7. Under VSA condition, four hypothetical Ln-MOFs offer higher APSs than their original structure YUSWIU (248 mol kg^{-1}), except Tm-furan (Table S7, ESI†). At PSA condition, La-furan, Tm-furan, Pr-oxadiazole, and Tm-oxadiazole have higher APSs (339, 298, 231, and 284 mol kg^{-1}, respectively) than YUSWIU (208 mol kg^{-1}). Overall, considering all the calculated performance metrics obtained using two different methodologies, and considering the notable difference between calculated $S_{ads,CO_2/N_2}$ at 10 bar for Pr-oxadiazole, we identified La-furan and Tm-oxadiazole as novel Ln-MOF candidates with improved APS values both at VSA and PSA conditions.

We finally compared the CO_2/N_2 separation performances of the Ln-MOFs that we generated in this work with the promising MOFs and COFs reported in the literature. The CO_2/N_2 selectivities of Zn-MOF-74, Ti-MIL-91, Cu-TDPAT, UTSA-16, and SIFSIX-3-Ni for the separation of CO_2/N_2: 15/85 mixture were computed as 63, 92, 214, 246, and 285, respectively, using the results of GCMC simulations.[68] Similarly, simulated CO_2/N_2 selectivities of the top-performing COFs for the CO_2/N_2: 15/85 mixture were computed as 14–40 and 6–19 at 1 bar and 10 bar, respectively.[69] In experiments, single-component gas adsorption measurements were performed for Mg-MOF-74,[70] SMOF-SIFSIX-1,[71] MIL-53(Al),[72] Ni-AG5,[73] MOF-505,[74] and MIL-101(Cr)[72] and CO_2/N_2 selectivities for the separation of CO_2/N_2: 15/85 mixture were predicted by the ideal adsorbed solution theory (IAST) as 150, 132, 64, 52, 37, and 8 at 1 bar, respectively. Our results showed that the modified Ln-MOFs could achieve CO_2/N_2 mixture selectivities up to 200 both at 1 and 10 bar, which are comparable to or better than those reported in the literature.

We proposed a computational workflow (Fig. 1) as an ideal scheme for the selection of promising Ln-MOFs for CO_2 capture and the design of better performing materials by the linker and metal node modification. Since screening thousands of MOFs with high precision is computationally very demanding, we used several assumptions, and our results should be evaluated under the validity of these assumptions. Ln-MOFs were assumed to be rigid in our molecular simulations, a widely

used assumption in the literature, to save computational time for studying a large number of materials. Recent studies showed that molecular adsorption is only weakly affected by the inclusion of MOFs' flexibility and considering the framework flexibility primarily affects the diffusion properties of gas molecules in MOFs.[46,75,76] For more realistic simulations, MOFs should be modeled as flexible frameworks in simulations in future studies.

Another assumption is related to the assignment of the partial atomic charges since the accuracy of the electrostatic interactions is strongly dependent on the charges of the atoms that make up the system. We note that partial atomic charges are not physically observable and there are several atomic charge assignment schemes. The charges can be derived from the electron wave function, electron density, electrostatic potential, or semi-empirical approaches.[77] Although DFT-derived charges are more accurate than the semi-empirical charge methods, it is not realistic to screen thousands of MOFs by computationally demanding DFT-derived charges. Thus, in this work, we used semi-empirically derived Q_{eq} charges to initially screen 2288 Ln-MOFs to obtain fast and reliable results, and then we performed a more detailed analysis for the 5 Ln-MOFs which appeared as the most promising materials for CO_2/N_2 separation, by assigning computationally demanding DFT-derived PACMOF charges to obtain more accurate results. The gas uptakes and adsorption selectivities of MOFs were shown to vary with the charge method used,[78,79] and in this study, we observed the presence of notable differences between CO_2 and N_2 uptakes of Q_{eq} and PACMOF-charged Ln-MOFs in some cases.

Another assumption we used in this study concerns the level of theory to be used in geometry optimizations of generated Ln-MOFs. Following the computational generation of a hypothetical MOF, the geometry should be optimized to obtain a more realistic geometry close to a local minima on the potential energy surface. Depending on the choice of the level of theory (such as force field, DFT functional/basis set, smearing procedure, convergence tolerance quality, *etc.*), the self-consistent field (SCF)

convergence may appear as a difficult task to achieve. Especially when the material includes lanthanide atoms, filling electrons in 4f-orbitals makes the calculations very complicated, and thus, increasing the SCF iterations up to tens of thousands may be needed,[80] which in turn significantly increases the computational time. Since the optimization of a large number of generated Ln-MOFs at the QM level appears to be unrealistic, we optimized the generated 77 Ln-MOFs at a faster MM-level for the initial screening in this work. The geometric parameters of MOFs were predicted well by this method in previous studies.[18] Then 5 Ln-MOFs, identified as the most promising materials, were optimized at the QM-level to obtain more reasonable geometrical parameters. The validities of our geometry optimization methods were checked by comparing the results with the experimentally reported structural parameters of YUSWIU. While the unit cell parameters of the MM-level optimized YUSWIU deviated less than 4.7%, QM-level optimized YUSWIU deviated to a maximum of 2.7%. Overall, our proposed workflow given in Fig. 1 works well within the limits of the assumptions that we discussed. We believe that this methodology can be useful for future studies, helping to identify key challenges and guide improvements in the screening and design of novel materials.

We finally note that it is crucial to address the synthesizability and stability of the top-performing adsorbents, as these Ln-MOFs are currently hypothetical. Recent studies have demonstrated that hypothetical MOFs can be synthesized since they are constructed using linkers similar to those available in the experimentally realized MOFs.[25,81] Future experimental studies are required to show the synthesizability and stability of the hypothetical Ln-MOFs that we computationally generated.

4. Conclusions

In this study, we presented a multi-level computational approach for generating high-performing hypothetical Ln-MOFs and testing them for adsorption-based CO_2/N_2 separation. A promising Ln-MOF, YUSWIU, having a moderate CO_2/N_2 selectivity was initially identified from the MOF database based on the results of molecular simulations, and then modified by linker and metal exchanges to generate 77 new hypothetical Ln-MOFs. After MM-level geometry optimization of these materials, 5 hypothetic Ln-MOFs which outperform the original YUSWIU in terms of selectivity and/or APS under VSA and PSA conditions were further optimized at QM-level and separation performances of these computer-generated MOFs were examined. La-furan and Tm-oxadiazole were identified as novel materials for CO_2/N_2 separation with very high APSs (334 and 409 mol kg^{-1} for VSA, 339 and 284 mol kg^{-1} for PSA, respectively) and selectivities (161 and 188 at 1 bar, 99 and 108 at 10 bar, respectively). Calculated Q_{st} values and adsorption snapshots obtained from molecular simulations indicated that oxygen atoms on the carboxylate ends, furan, and oxadiazole rings are the most attractive sites for both gases, whereas nitrogen atoms on oxadiazole rings were found to be attractive for only CO_2. The repulsive oxadiazole rings for N_2 decrease the affinity of N_2,

allowing Ln-MOFs generated from 1,3,4-oxadiazole-2,5-dicarboxylate linkers to be more CO_2 selective than furan-2,5-dicarboxylate linkers. Thus, hypothetical Pr-oxadiazole, Sm-oxadiazole, and Tm-oxadiazole were found to outperform the parent MOF, YUSWIU (Dy-furan), in terms of selectivity and APS, especially under VSA condition, because of their CO_2 attractive and N_2 repulsive 1,3,4-oxadiazole-2,5-dicarboxylate linkers. On the other hand, Ln nodes were observed to alter the electronic nature of the coordinating oxygens, allowing them to be richer in electrons, and vary the porosity of the MOF. When the Dy^{3+} nodes in YUSWIU were changed with La^{3+} (La-furan), the larger porosity of La-furan allowed more CO_2 molecules to be adsorbed, making La-furan more CO_2/N_2 selective than YUSWIU. Considering the robustness of the results obtained from MM and QM-level calculations, Tm-oxadiazole and La-furan were proposed as promising adsorbents for CO_2/N_2 separation under VSA and PSA conditions.

Author contributions

ZPH: methodology, software, validation, investigation, conceptualization, writing – original draft, writing – review & editing. HCG: methodology, software, validation, investigation, conceptualization, writing – original draft, writing – review & editing. SK: conceptualization, supervision, methodology, writing – original draft, writing – review & editing.

Data availability

The data supporting this article have been included as part of the ESI† and five cifs are available at Zenodo at **https://doi.org/10.5281/zenodo.14616175**.

Conflicts of interest

There are no conflicts to declare.

Acknowledgements

References

1 G. P. Peters, R. M. Andrew, J. G. Canadell, P. Friedlingstein, R. B. Jackson, J. I. Korsbakken, C. Le Quéré and A. Peregon, *Nat. Clim. Change*, 2020, **10**, 3–6.

2 J. F. Brennecke and B. E. Gurkan, *J. Phys. Chem. Lett.*, 2010, **1**, 3459–3464.

3 M. Oschatz and M. Antonietti, *Energy Environ. Sci.*, 2018, **11**, 57–70.

4 L. B. Hamdy, C. Goel, J. A. Rudd, A. R. Barron and E. Andreoli, *Mater. Adv.*, 2021, **2**, 5843–5880.

5 S. Kitagawa, *Chem. Soc. Rev.*, 2014, **43**, 5415–5418.

6 B. Yeskendir, J.-P. Dacquin, Y. Lorgouilloux, C. Courtois, S. Royer and J. Dhainaut, *Mater. Adv.*, 2021, **2**, 7139–7186.

7 R. Das, D. Muthukumar, R. S. Pillai and C. M. Nagaraja, *Chem. – Eur. J.*, 2020, **26**, 17445–17454.

8 B. Arstad, H. Fjellvåg, K. O. Kongshaug, O. Swang and R. Blom, *Adsorption*, 2008, **14**, 755–762.

9 H. Li, K. Wang, D. Feng, Y. P. Chen, W. Verdegaal and H. C. Zhou, *ChemSusChem*, 2016, **9**, 2832–2840.

10 Z. Lu, J. Bai, C. Hang, F. Meng, W. Liu, Y. Pan and X. You, *Chem. – Eur. J.*, 2016, **22**, 6277–6285.

11 S. Wang, H. Reinsch, N. Heymans, M. Wahiduzzaman, C. Martineau-Corcos, G. De Weireld, G. Maurin and C. Serre, *Matter*, 2020, **2**, 440–450.

12 D. H. Hong and M. P. Suh, *Chem. – Eur. J.*, 2014, **20**, 426–434.

13 Y. W. Abraha, C.-W. Tsai, J. H. Niemantsverdriet and E. H. Langner, *ACS Omega*, 2021, **6**, 21850–21860.

14 X. Wu, Z. Bao, B. Yuan, J. Wang, Y. Sun, H. Luo and S. Deng, *Microporous Mesoporous Mater.*, 2013, **180**, 114–122.

15 C. R. Wade and M. Dincă, *Dalton Trans.*, 2012, **41**, 7931–7938.

16 S. Waitschat, D. Fröhlich, H. Reinsch, H. Terraschke, K. Lomachenko, C. Lamberti, H. Kummer, T. Helling, M. Baumgartner and S. Henninger, *Dalton Trans.*, 2018, **47**, 1062–1070.

17 G. Avci, S. Velioglu and S. Keskin, *J. Phys. Chem. C*, 2019, **123**, 28255–28265.

18 J. Borycz, D. Tiana, E. Haldoupis, J. C. Sung, O. K. Farha, J. I. Siepmann and L. Gagliardi, *J. Phys. Chem. C*, 2016, **120**, 12819–12830.

19 G. Avci, C. Altintas and S. Keskin, *J. Phys. Chem. C*, 2021, **125**, 17311–17322.

20 Z. Qiao, N. Wang, J. Jiang and J. Zhou, *Chem. Commun.*, 2016, **52**, 974–977.

21 S. Li, Y. G. Chung, C. M. Simon and R. Q. Snurr, *J. Phys. Chem. Lett.*, 2017, **8**, 6135–6141.

22 S. Surblé, C. Serre, C. Mellot-Draznieks, F. Millange and G. Férey, *Chem. Commun.*, 2006, 284–286.

23 N. T. X. Huynh, O. K. Le, T. P. Dung and V. Chihaia, *RSC Adv.*, 2023, **13**, 15606–15615.

24 R. L. Martin, L.-C. Lin, K. Jariwala, B. Smit and M. Haranczyk, *J. Phys. Chem. C*, 2013, **117**, 12159–12167.

25 M. Witman, S. Ling, S. Anderson, L. Tong, K. C. Stylianou, B. Slater, B. Smit and M. Haranczyk, *Chem. Sci.*, 2016, **7**, 6263–6272.

26 D. A. Gomez-Gualdron, O. V. Gutov, V. Krungleviciute, B. Borah, J. E. Mondloch, J. T. Hupp, T. Yildirim, O. K. Farha and R. Q. Snurr, *Chem. Mater.*, 2014, **26**, 5632–5639.

27 X. Wang, L. Zhang, J. Yang, F. Liu, F. Dai, R. Wang and D. Sun, *J. Mater. Chem. A*, 2015, **3**, 12777–12785.

28 Y. Cui, B. Chen and G. Qian, *Coord. Chem. Rev.*, 2014, **273**, 76–86.

29 B. Yan, *Inorg. Chem. Front.*, 2021, **8**, 201–233.

30 Y. Zhang, S. Liu, Z.-S. Zhao, Z. Wang, R. Zhang, L. Liu and Z.-B. Han, *Inorg. Chem. Front.*, 2021, **8**, 590–619.

31 Z. Qiao, K. Zhang and J. Jiang, *J. Mater. Chem. A*, 2016, **4**, 2105–2114.

32 B.-B. Xing, Y.-S. Wang, T. Zhang, J.-Y. Liu, H. Jiao and L. Xu, *Mater. Adv.*, 2025, **6**, 756–765.

33 A. Zulys, F. Yulia, A. Buhori, N. Muhadzib, M. Ghiyats and B. B. Saha, *J. Mater. Res. Technol.*, 2020, **9**, 7409–7417.

34 Q. Yao, A. Bermejo Gómez, J. Su, V. Pascanu, Y. Yun, H. Zheng, H. Chen, L. Liu, H. N. Abdelhamid and B. N. Martín-Matute, *Chem. Mater.*, 2015, **27**, 5332–5339.

35 Y. Chen and S. Ma, *Rev. Inorg. Chem.*, 2012, **32**, 81–100.

36 D. H. Le, R. P. Loughan, A. Gładysiak, N. Rampal, I. A. Brooks, A.-H. A. Park, D. Fairen-Jimenez and K. C. Stylianou, *J. Mater. Chem. A*, 2022, **10**, 1442–1450.

37 Z. Lin, R. Zou, J. Liang, W. Xia, D. Xia, Y. Wang, J. Lin, T. Hu, Q. Chen and X. Wang, *J. Mater. Chem.*, 2012, **22**, 7813–7818.

38 S. Pal, A. Bhunia, P. P. Jana, S. Dey, J. Möllmer, C. Janiak and H. P. Nayek, *Chem. – Eur. J.*, 2015, **21**, 2789–2792.

39 W. Mu, X. Huang, R. Zhong, W. Xia, J. Liu and R. Zou, *CrystEngComm*, 2015, **17**, 1637–1645.

40 H. Daglar and S. Keskin, *J. Phys. Chem. C*, 2018, **122**, 17347–17357.

41 Y. G. Chung, E. Haldoupis, B. J. Bucior, M. Haranczyk, S. Lee, H. Zhang, K. D. Vogiatzis, M. Milisavljevic, S. Ling and J. S. Camp, *J. Chem. Eng. Data*, 2019, **64**, 5985–5998.

42 T. F. Willems, C. H. Rycroft, M. Kazi, J. C. Meza and M. Haranczyk, *Microporous Mesoporous Mater.*, 2012, **149**, 134–141.

43 D. Dubbeldam, S. Calero, D. E. Ellis and R. Q. Snurr, *Mol. Simul.*, 2016, **42**, 81–101.

44 A. K. Rappe and W. A. Goddard III, *J. Phys. Chem.*, 1991, **95**, 3358–3363.

45 C. E. Wilmer and R. Q. Snurr, *Chem. Eng. J.*, 2011, **171**, 775–781.

46 C. Altintas and S. Keskin, *ACS Sustainable Chem. Eng.*, 2018, **7**, 2739–2750.

47 Z. Qiao, C. Peng, J. Zhou and J. Jiang, *J. Mater. Chem. A*, 2016, **41**, 15904–15912.

48 A. K. Rappé, C. J. Casewit, K. Colwell, W. A. Goddard III and W. M. Skiff, *J. Am. Chem. Soc.*, 1992, **114**, 10024–10035.

49 B. L. Eggimann, A. J. Sunnarborg, H. D. Stern, A. P. Bliss and J. I. Siepmann, *Mol. Simul.*, 2014, **40**, 101–105.

50 C. Murthy, K. Singer, M. Klein and I. McDonald, *Mol. Phys.*, 1980, **41**, 1387–1399.

51 P. P. Ewald, *Ann. Phys.*, 1921, **369**, 253–287.

52 T. Vlugt, E. García-Pérez, D. Dubbeldam, S. Ban and S. Calero, *J. Chem. Theory Comput.*, 2008, **4**, 1107–1118.

53 C. F. Macrae, I. Sovago, S. J. Cottrell, P. T. Galek, P. McCabe, E. Pidcock, M. Platings, G. P. Shields, J. S. Stevens and M. Towler, *Appl. Crystallogr.*, 2020, **53**, 226–235.

54 D. S. Biovia, Dassault Systèmes: San Diego, BW, Release, 2017.

55 B. Delley, *J. Chem. Phys.*, 1990, **92**, 508–517.

56 B. Delley, *J. Chem. Phys.*, 2000, **113**, 7756–7764.

57 M. Ernzerhof and G. E. Scuseria, *J. Chem. Phys.*, 1999, **110**, 5029–5036.

58 A. D. Becke, *Phys. Rev. A:At., Mol., Opt. Phys.*, 1988, **38**, 3098.

59 C. Lee, W. Yang and R. G. Parr, *Phys. Rev. B:Condens. Matter Mater. Phys.*, 1988, **37**, 785.

60 S. Kancharlapalli, A. Gopalan, M. Haranczyk and R. Q. Snurr, *J. Chem. Theory Comput.*, 2021, **17**, 3052–3064.

61 T. A. Manz and D. S. Sholl, *J. Chem. Theory Comput.*, 2010, **6**, 2455–2468.

62 K. Liu, H. Li, X. Zhang, W. Shi and P. Cheng, *Inorg. Chem.*, 2015, **54**, 10224–10231.

63 S. C. Bart, *Inorg. Chem.*, 2023, **62**(9), 3713–3714.

64 D. Ko, H. A. Patel and C. T. Yavuz, *Chem. Commun.*, 2015, **51**, 2915–2917.

65 D. Nazarian, J. S. Camp, Y. G. Chung, R. Q. Snurr and D. S. Sholl, *Chem. Mater.*, 2017, **29**, 2521–2528.

66 G. O. Aksu, I. Erucar, Z. P. Haslak and S. Keskin, *J. CO2 Util.*, 2022, **62**, 102077.

67 H. C. Gulbalkan, Z. P. Haslak, C. Altintas, A. Uzun and S. Keskin, *Sep. Purif. Technol.*, 2022, **287**, 120578.

68 D. Yancy-Caballero, K. T. Leperi, B. J. Bucior, R. K. Richardson, T. Islamoglu, O. K. Farha, F. You and R. Q. Snurr, *Mol. Syst. Des. Eng.*, 2020, **5**, 1205–1218.

69 O. F. Altundal, C. Altintas and S. Keskin, *J. Mater. Chem. A*, 2020, **8**, 14609–14623.

70 J. A. Mason, K. Sumida, Z. R. Herm, R. Krishna and J. R. Long, *Energy Environ. Sci.*, 2011, **4**, 3030–3040.

71 J. Dai, D. Xie, Y. Liu, Z. Zhang, Y. Yang, Q. Yang, Q. Ren and Z. Bao, *Ind. Eng. Chem. Res.*, 2020, **59**, 7866–7874.

72 N. Singh, S. Dalakoti, A. Sharma, R. Chauhan, R. S. Murali, S. Divekar and S. Dasgupta, *Sep. Purif. Technol.*, 2024, **341**, 126820.

73 L. Asgharnejad, A. Abbasi and A. Shakeri, *Microporous Mesoporous Mater.*, 2018, **262**, 227–234.

74 Y. Chen, D. Lv, J. Wu, J. Xiao, H. Xi, Q. Xia and Z. Li, *Chem. Eng. J.*, 2017, **308**, 1065–1072.

75 I. Erucar and S. Keskin, *J. Membr. Sci.*, 2016, **514**, 313–321.

76 E. Haldoupis, T. Watanabe, S. Nair and D. S. Sholl, *ChemPhysChem*, 2012, **13**, 3449–3452.

77 M. Cho, N. Sylvetsky, S. Eshafi, G. Santra, I. Efremenko and J. M. Martin, *ChemPhysChem*, 2020, **21**, 688–696.

78 C. Cleeton, F. L. de Oliveira, R. F. Neumann, A. H. Farmahini, B. Luan, M. Steiner and L. Sarkisov, *Energy Environ. Sci.*, 2023, **16**, 3899–3918.

79 C. Altintas and S. Keskin, *Mol. Syst. Des. Eng.*, 2020, **5**, 532–543.

80 V. A. Basiuk, *Comput. Theor. Chem.*, 2025, 115170.

81 P. G. Boyd, A. Chidambaram, E. García-Díez, C. P. Ireland, T. D. Daff, R. Bounds, A. Gładysiak, P. Schouwink, S. M. Moosavi and M. M. Maroto-Valer, *Nature*, 2019, **576**, 253–256.